Exciton Collimation, Focusing and Trapping Using Complex Transition Metal Dichalcogenide Lateral Heterojunctions

Hassan Lamsaadi, Aurelien Cuche, Gonzague Agez, Ioannis Paradisanos, Dorian Beret, Laurent Lombez, Pierre Renucci, Delphine Lagarde, Xavier Marie, Ziyang Gan, et al.

ADVANCED OPTICAL MATERIALS
www.advopticalmat.de

Exciton Collimation, Focusing and Trapping Using Complex Transition Metal Dichalcogenide Lateral Heterojunctions

*Hassan Lamsaadi, Aurelien Cuche, Gonzague Agez, Ioannis Paradisanos, Dorian Beret, Laurent Lombez, Pierre Renucci, Delphine Lagarde, Xavier Marie, Ziyang Gan, Antony George, Kenji Watanabe, Takashi Taniguchi, Andrey Turchanin, Nicolas Combe, Bernhard Urbaszek, Vincent Paillard, and Jean-Marie Poumirol**

Controlling the motion of neutral excitons in optically active media is a mandatory development to enable the conception of advanced circuits and devices for applications in excitronics, quantum photonics, and optoelectronics. Recently, proof of unidirectional exciton transport from high- to low-bandgap material is evidenced using a high-quality lateral heterostructure separating transition metal dichalcogenide monolayers (TMD-MLs). In this paper, by combining room-temperature micro-photoluminescence far-field imaging with a statistical description of exciton transport, the underlying excitonic local distribution and fluxes taking place near lateral heterojunctions are unveiled. The complex 2D excitonic transport properties found near a linear interface separating WSe_2 from $MoSe_2$ TMD-MLs are studied and reveal two distinct diffusion regimes profoundly affecting the effective diffusion length. Then, it is shown that combining two and three of these interfaces, allows advanced in-plane control of the excitonic distribution and flux over large distances. Exciton focalization and trapping, allowing an increase in the local exciton density up to three orders of magnitude are demonstrated. Finally, flux collimation is achieved with the formation of parallel current lines extending a few micrometers away from the source. We believe that the deterministic shaping and positioning of the exciton distribution and flux shown here will be key toward the conception of realistic excitronic devices.

1. Introduction

Atomically-thin semiconductors have been at the center of a very active research field in recent years thanks to their remarkable optical properties. In particular, transition metal dichalcogenide monolayers (TMD-MLs) exhibit a strong Coulomb interaction, resulting in the formation of tightly bound neutral excitons that are highly stable even at room temperature.[1–5] Furthermore, excitons in TMD-MLs allow optical signals to be encoded and stored in the exciton energy, spin, valley, and orbital degrees of freedom,[6,7] and they can propagate over hundreds of nanometers before recombining. As a result, TMD-MLs provide an ideal platform for investigating exciton transport phenomena and are very promising candidates to be used in many quantum photonic and optoelectronic applications.

Excitronic circuits, similar to electronic circuits, using excitons as active information carriers have been anticipated to control excitonic states with applied electric and magnetic fields.[8,9] In addition,

H. Lamsaadi, A. Cuche, G. Agez, N. Combe, V. Paillard, J.-M. Poumirol
CEMES-CNRS
Université de Toulouse
29 Rue Jeanne Marvig, Toulouse 31055, France
E-mail: jean-marie.poumirol@cemes.fr

I. Paradisanos
Institute of Electronic Structure and Laser
Foundation for Research and Technology-Hellas
Heraklion 70013, Greece

The ORCID identification number(s) for the author(s) of this article can be found under https://doi.org/10.1002/adom.202403009

DOI: 10.1002/adom.202403009

D. Beret, L. Lombez, P. Renucci, D. Lagarde, X. Marie
Université de Toulouse
INSA-CNRS-UPS, LPCNO
135 Avenue Rangueil, Toulouse 31077, France

Z. Gan, A. George, A. Turchanin
Friedrich Schiller University Jena
Institute of Physical Chemistry
07743 Jena, Germany

A. George, A. Turchanin
Abbe Centre of Photonics
07745 Jena, Germany

K. Watanabe
Research Center for Functional Materials
National Institute for Materials Science
1-1 Namiki, Tsukuba 305-0044, Japan

T. Taniguchi
International Center for Materials Nanoarchitectonics
National Institute for Materials Science
1-1 Namiki, Tsukuba 305-0044, Japan

photo-excitonic state interactions can directly process optical signals and re-emit light without the need for additional optical-electrical conversions, making them extremely efficient.[10] Nevertheless, because of their neutral charge state, controlled spatial manipulation of neutral exciton fluxes at room temperature using electric or magnetic fields is challenging. Previous studies on manipulating exciton propagation focused mainly on the use of strained TMD-MLs.[11] The strain gradient obtained through rough nano-structured substrates is used, for example, for exciton funneling.[12]

Recently, an alternative method based on CVD-grown high-quality in-plane lateral heterostructures, combining TMD-MLs with different excitonic properties, has unveiled several fundamental behaviors and opened new perspectives.[13–16] For instance, a unidirectional exciton flow has been observed in high-quality WSe_2-$MoSe_2$ lateral heterojunction (LH), forming a diode-like junction (abrupt interface between two TMD-MLs with different band gaps).[17–19]

Excitons photo-generated within the larger bandgap TMD-ML near the interface are effectively drawn into the adjacent lower bandgap TMD-ML, facilitating their transfer across the junction. In contrast, excitons generated within the lower bandgap TMD-ML are confined and unable to cross the junction.[17] This phenomenon has been described using the concept of an excitonic Kapitza resistance-like effect, which accounts for a pronounced discontinuity in the excitonic distribution at the junction due to exciton drift (for an in-depth discussion, see ref. [19]). This effect is analogous to the Kapitza resistance observed during phonon transfer across ideal interfaces between two materials, where a temperature discontinuity similarly emerges at the interface.

Similar behavior has been observed in $WS_{2\xi}Se_{2-2\xi}$ alloy with gradually changing composition ξ, where the slowly varying exciton energy generates an anisotropic exciton drift and an increasing effective diffusion length.[20] However, all those works were focused on a quasi-1D diffusion observed on straight-line junctions. The understanding of how LHs could affect exciton diffusion and authorize control of their spatial motion in 2D space using more complex geometries is still lacking.

In this work, we go further by demonstrating that TMD-based lateral heterostructures, depending on their geometry, can profoundly modify the trajectory of excitons in a controllable way. This allows complex in-plane manipulation of exciton flux and distribution. By coupling achromatic μ-photoluminescence (μ-PL) microscopy imaging with homemade numerical simulation tools based on a statistical resolution of the randomly moving excitons, we show that a highly directional transfer of kinetic energy to the excitons when transmitted through the junction (from high band gap WSe_2 to low band gap $MoSe_2$) or reflected by the junction (from $MoSe_2$ to WSe_2) affects both their effective diffusion lengths and trajectories. First, we demonstrate that two different diffusion regimes exist in the vicinity of a linear (straight) LH, allowing either i) a strong enhancement of the effective diffusion length (nearly one order of magnitude) leading to efficient exciton transport far away from their source or ii) a regime of forced diffusion where excitons are forced to move toward high-density regions, leading to exciton condensation and negative effective diffusion length. Building on the determined transmission and reflection rules, we study the effect of more complex junction geometries near triangular interfaces. We demonstrate that the presence of two interacting interfaces (near triangular interfaces) generates an excitonic-like lensing effect, allowing, depending on the position of the exciton source, i) efficient collimation of the exciton trajectory or ii) the exciton population to be focused and concentrated at a controllable position away from the exciton source. Finally, we show that a subwavelength-sized $MoSe_2$ triangle inclusion in a WSe_2 ML drains excitons, thus acting as a trap from the surrounding barrier. The exciton density inside the trap is increased by nearly three orders of magnitude when the triangle size is reduced to a few hundred nanometers.

2. Results

2.1. μ-PL Study of $MoSe_2$-WSe_2 LH

High-quality $MoSe_2$-WSe_2 LH is grown using the modified CVD method described in ref. [16], then transferred and encapsulated in hexagonal boron nitride (hBN) on a SiO_2/Si substrate (see Methods in Supporting Information). Following each transfer step, the substrate is annealed at 150°C for 30 min to agglomerate any nanobubbles away from the junction. We exclusively worked with bubble-free junctions to preserve the intrinsic material properties and eliminate any additional drift of excitons due to strain from nanobubbles.[21] **Figure 1a** shows an optical image of the sample, with the top and bottom hBN flakes indicated by the orange and black lines, respectively. The top and bottom color maps in Figure 1b represent the normalized maxima of μ-PL and μ-Raman intensities, respectively. A star-shaped $MoSe_2$ inclusion (purple) surrounded by WSe_2 monolayer (pink) can be identified. The sample exhibits very few visible defects, mainly bilayer $MoSe_2$ inclusions at the center of the stars. Figure 1c illustrates the general atomic configuration at the vicinity of the junction, with the two pure materials WSe_2 (pink) and $MoSe_2$ (purple) separated by a junction of width w. The junction is considered to be formed of a $Mo_\xi W_{1-\xi} Se_2$ alloy with a continuous but abruptly varying composition from $MoSe_2$ (left) to WSe_2 (right), resulting in a continuously and abruptly varying exciton energy profile as described by Figure 1c.[22] As it will be discussed later, the exact nature of the junction is not crucial for the description of our experimental results, as in our case we studied abrupt junctions (narrow width $w < 10$ nm).

To determine the effect of the junction on the exciton diffusion, we performed μ-PL imaging experiments, sequentially imaging the PL emission pattern and analyzing the collected light with a spectrometer. Figure 1d shows an illustration of the experimental setup. We point out that the laser is tightly focused through a high numerical aperture (NA = 0.9), and the emitted light is collected by the same objective through a confocal hole of controllable size (see Methods in Supporting Information). All measurements were made at low power density (below 1×10^9 W cm^{-2}) to ensure that the excitonic diffusion regime is linear.[19] **Figure 2a** upper row depicts the μ-PL images for six selected positions of the laser excitation recorded along a line perpendicular to the

B. Urbaszek
Institute of Condensed Matter Physics
Technische Universität Darmstadt
64289 Darmstadt, Germany

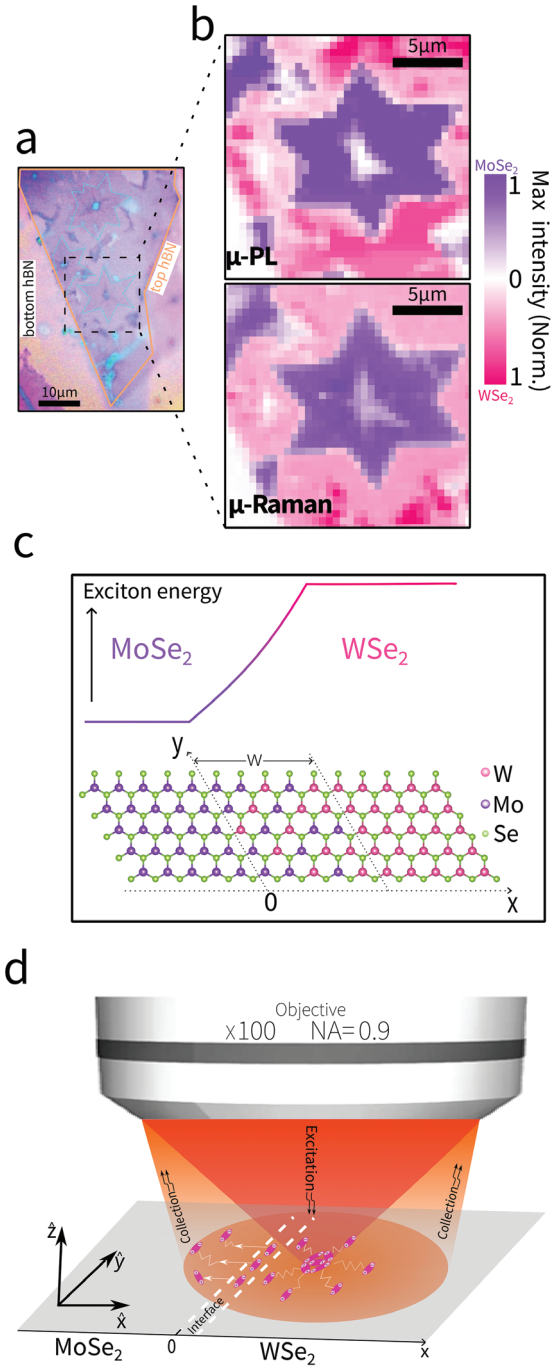

Figure 1. μ-PL and μ-Raman characterization of the sample. a) Optical image of the hBN/TMD-LH/hBN stack. The top hBN flake boundaries are indicated by the orange solid line (the bottom hBN flake covers the whole image, delimited by the black rectangle). The dashed cyan lines show the lateral heterojunctions between a star-shaped $MoSe_2$ monolayer embedded in a WSe_2 monolayer. b) Top and bottom color maps represent the normalized maxima of μ-PL and μ-Raman intensities, respectively. The color maps are taken inside the square zone (dashed black line) in a. The purple (pink) color corresponds to the $MoSe_2$ (WSe_2) signal. c) Schematic representation of an abrupt $MoSe_2$-WSe_2 LH showing a thin interface (of width w) with a continuous varying alloy composition, where the exciton energy continuously increases from the exciton energy inside $MoSe_2$ to the exciton energy inside WSe_2. d) Illustration of the μ-PL imaging set-up.

$MoSe_2$-WSe_2 LH. As a guide for the eyes and for clarity, the laser spot is indicated by the dashed red circle with a diameter equal to the experimentally measured full width at half maximum, FWHM~1 μm. The corresponding μ-PL spectra appear in Figure 2b. In Figure 2a, panels (1) and (6) show μ-PL images with the laser spot far from the junction, corresponding to the pure exciton emission of $MoSe_2$ and WSe_2, respectively. This is confirmed by the spectral signatures. For $MoSe_2$ (panel (1) of Figure 2b), the spectrum corresponds to the neutral exciton $A_{1s}^{MoSe_2}$ centered around ~1.57 eV (FWHM ≈ 50 meV). For WSe_2 (panel (6) of Figure 2b), an asymmetric spectrum exhibits the contribution of the dark exciton X_D centered ≈1.62 eV (FWHM ≈ 30 meV), in addition to the dominant feature of the neutral exciton $A_{1s}^{WSe_2}$ centered around ≈1.66 eV (FWHM ≈ 40 meV).[23–25] In addition, WSe_2 is much brighter than $MoSe_2$ (≈3 times), and both patterns reveal a clear isotropic diffusion in each material, with the μ-PL intensity maximum position matching the laser excitation center. This is confirmed by the 1D profiles taken from the corresponding μ-PL images (panels 1 and 6) presented in Figure 2a lower row. Those profiles show the variation along the x-axis of the integrated intensity ($I_{PL}(x, x_{laser}) = \int dy I_{PL}(x, y, x_{laser})$), calculated by integrating along the y-axis the μ-PL intensity of the 2D maps ($I_{PL}(x, y, x_{laser})$). This is in agreement with symmetric exciton effective diffusion lengths of $L_D^{WSe_2} \sim 90$ nm and $L_D^{MoSe_2} \sim 142$ nm, aligned with the previous studies on the same kind of samples.[17,19]

A very interesting and complex behavior takes place when moving the laser across the junction from $MoSe_2$ to WSe_2 (panels 2 to 5 in Figure 2a). The intensity pattern is strongly modified depending on the relative position of the laser excitation with respect to the junction (Figure S1, Supporting Information illustrates the method used to estimate the junction position). In panel (2), only the laser spot edge is illuminating the junction, but a sensitive increase of the PL pattern broadening along the x-axis toward WSe_2 can be seen (especially compared to the laser spot size), a sign of an enhanced effective diffusion length along that direction. In panel (3), the broadening is further increased, with the appearance of two distinct maxima. One of them nearly matches the position of the laser excitation center, while the other maximum appears near the position of the junction, making the μ-PL intensity pattern strongly asymmetric. To quantify the spatial broadening of the PL distribution, we use the Full Width at Outer Half Maximum (FWOHM), defined as the distance between the outermost points where the intensity drops to half of the maximum value, providing a robust measure applicable to both unimodal and bimodal distributions. In the configuration (3), the FWOHM of the μ-PL spot is reaching 1500 nm, ≈1.5 times larger than the one observed in (1) and (6). In panel (4), we emphasize that the asymmetry of the μ-PL intensity pattern is further increased, and that the PL intensity maximum is no longer matching the laser center. It is shifted by ≈400 nm along the x-axis toward the WSe_2 side of the junction, while a shoulder is still visible deep inside the $MoSe_2$ side. When further increasing the proportion of laser excitation occurring inside WSe_2 (laser spot center close to the junction as in panel (5)), an abrupt change of the μ-PL intensity pattern is observed: the maximum of the μ-PL intensity is still pushed away from the junction (by ≈150 nm), and the PL spot shrinks to a size smaller than the laser excitation

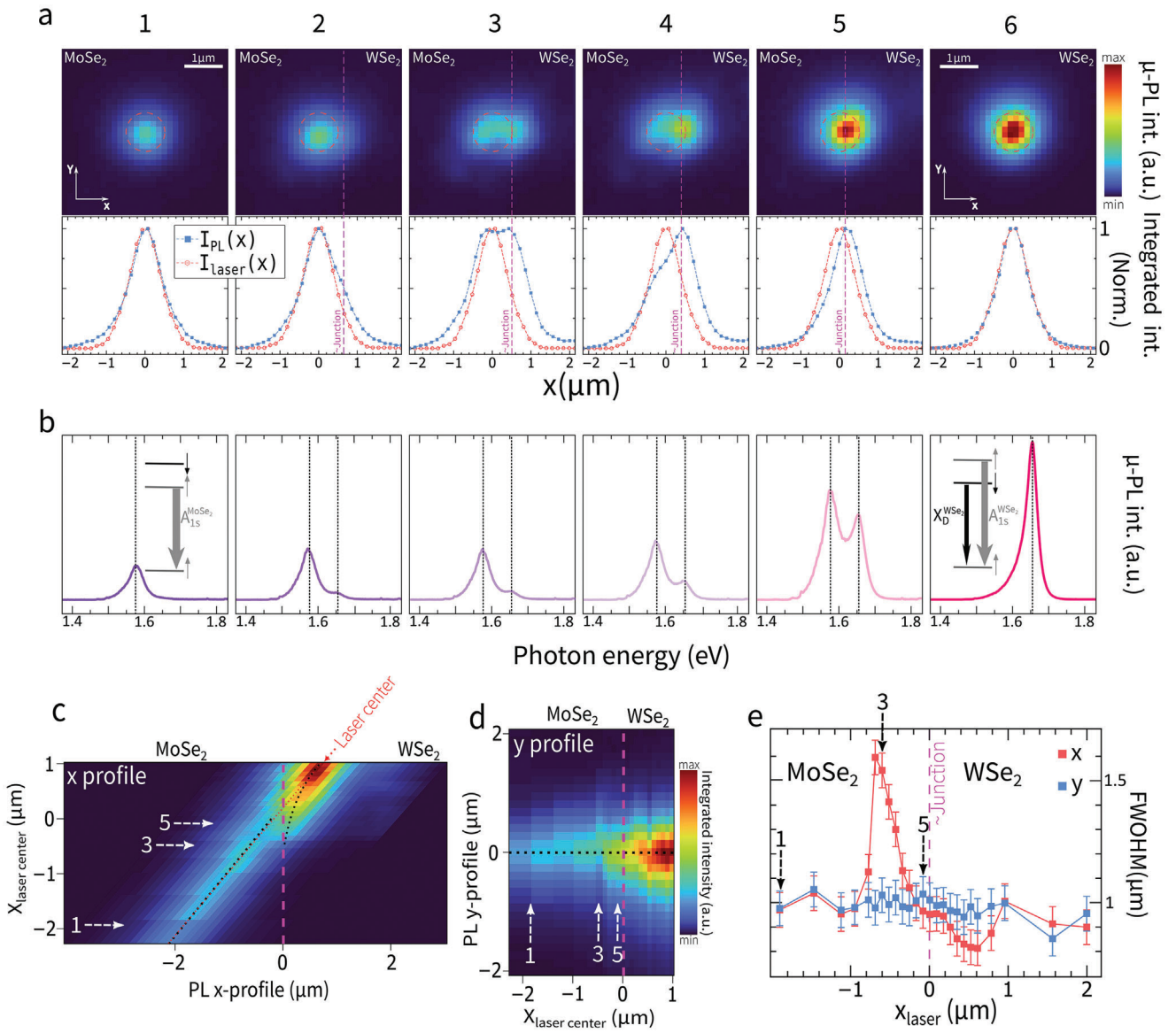

Figure 2. μ-PL imaging experiment of exciton diffusion through $MoSe_2$-WSe_2 LH. a) Top panels: μ-PL images measured away from the junction in $MoSe_2$ (1) and in WSe_2 (6), and close to the junction (2 to 5). The dashed red circle, with a diameter of *FWHM* ~ 1μm, indicates the position of the excitation laser spot, and the dashed purple line indicates the estimated position of the junction separating $MoSe_2$ and WSe_2. The pixels appearing on the images are the actual pixels of the camera used to image the μ-PL. Bottom panels: *x*-axis profiles taken from the corresponding intensity maps. Blue curves: integrated μ-PL intensity $I_{PL}(x, x_{laser}) = \int dy I_{PL}(x, y, x_{laser})$; red curves: integrated intensity profile of the laser spot ($I_{laser}(x) = \int dy I_{laser}(x, y)$). b) μ-PL spectra measured at positions (1) to (6). Insets: illustration of different exciton transitions in $MoSe_2$ and WSe_2. c) Color map obtained from plotting the integrated μ-PL intensity $I_{PL}(x, x_{laser}) = \int dy I_{PL}(x, y, x_{laser})$) profiles (as displayed in a bottom panels) as a function of the position of the excitation source (center of the laser spot shown by the diagonal dotted red line), the dotted black line shows the position of the integrated intensity maximum. The vertical dashed line represents the separation between the two materials. d. Same as c but for integrated μ-PL intensity $I_{PL}(y, x_{laser}) = \int dx I_{PL}(x, y, x_{laser})$. e Full Width at Outer Half Maximum (FWOHM) of the integrated intensity profiles $I_{PL}(x, x_{laser})$ (red) and $I_{PL}(y, x_{laser})$ (blue) as a function of the position of the laser center. FWOHM is defined as the distance between the outermost points where the intensity drops to half of the maximum.

profile. Note that the behavior described here is typical and appears when scanning other junctions on the sample (see Figure S2a, Supporting Information).

Except for positions (1) and (6) far from the junction, the spectra measured on all other positions (see Figure 2b) show both signatures of WSe_2 and $MoSe_2$ materials, with various intensity ratio, which means that excitons are recombining on each side of the junction. It is interesting to note that neither $A_{1s}^{WSe_2}$ nor $A_{1s}^{MoSe_2}$ energy and broadening are affected by the presence of the junction. This is a good indication that the junction is very sharp, and the alloying region between the two materials, if any, is very small (in agreement with TEM image shown in ref. [17]). Furthermore, as the laser excitation approaches the junction from

$MoSe_2$ side, the PL intensity of $MoSe_2$ nearly triples before going to zero when the excitation laser takes place exclusively inside WSe_2 (see PL spectra in Figure 2c). This increase of $MoSe_2$ PL intensity confirms that the junction efficiently drives and accelerates excitons toward $MoSe_2$.[19] Finally, as expected for room temperature measurements, no signature of charge transfer excitons can be detected.[26]

To go further and confirm that the local exciton density can be strongly modified near the junction and that this modification occurs only in the direction perpendicular to the junction, the color map in Figure 2c gives the integrated intensity profiles $I_{PL}(x, x_{laser}) = \int dy I_{PL}(x, y, x_{laser})$ as a function of the laser position. Unambiguously, close to the interface, the PL spot splits into two peaks, generalizing the results shown in the six profiles displayed in Figure 2a. In contrast, the color map in Figure 2d showing the integrated intensity profiles $I_{PL}(y, x_{laser}) = \int dx I_{PL}(x, y, x_{laser})$ exhibits a single maximum always matching the laser center, proving that the junction does not influence the exciton distribution along the y-axis. Figure 2e shows the experimental FWOHM of the μ-PL spot. The red curve (blue curve) displays the FWOHM along the x-direction (y-direction). One can clearly see that, near the junction, two areas with very different diffusion regimes appear. First, an enhanced effective diffusion regime, where the FWOHM of the PL spot along the x-axis (red curve) is strongly increased by up to 50% compared to the y-axis FWOHM (blue curve), effectively spreading the PL spot. Second, a forced effective diffusion regime, where the FWOHM of the PL spot along the x-axis now becomes smaller than the one measured along the y-axis (the red curve going above the blue curve). The measured FWOHM goes down to 800 nm, meaning that along the x-direction, the μ-PL spot is smaller than the laser spot which is very surprising and cannot be explained without accounting for a strongly an-isotropic diffusion.

2.2. Statistical Approach of Exciton Diffusion

In this section, we develop a model that describes the effect of the junction on the exciton distribution to explain the complex behavior of the experimental μ-PL profile described above. We use a statistical approach to solve, in the linear regime, the following 2D diffusion equation:

$$-\vec{\nabla}.\left(-D(\mathbf{r})\vec{\nabla}n(\mathbf{r},\mathbf{r}_s,t)+\vec{v}^*(\mathbf{r})n(\mathbf{r},\mathbf{r}_s,t)\right)-\frac{n(\mathbf{r},\mathbf{r}_s,t)}{\tau(\mathbf{r})}+\Gamma(\mathbf{r},\mathbf{r}_s)=\frac{\partial n(\mathbf{r},\mathbf{r}_s,t)}{\partial t} \quad (1)$$

where $n(\mathbf{r}, \mathbf{r}_s, t)$ represents the time-dependent exciton density at the $\mathbf{r}(x, y)$ position with the excitation source centered at the $\mathbf{r}_s(x_{laser}, y_{laser})$ position. $D(\mathbf{r})$ and $\tau(\mathbf{r})$ are the intrinsic diffusion coefficient and lifetime of exciton, respectively.

In the left-hand side of Equation 1, the first term $-D(\mathbf{r})\vec{\nabla}n(\mathbf{r},\mathbf{r}_s,t)$ represents the diffusion flux and $\vec{v}^*(\mathbf{r})n(\mathbf{r},\mathbf{r}_s,t)$ the drift flux through the junction. Indeed, the exciton reaching the junction acquires a velocity directed from the high-bandgap material toward the low-bandgap material and related to its energy-variation, $\Delta E = E_{WSe_2} - E_{MoSe_2}$. We assume for the purpose of the model that the exciton energy varies continuously following Vegard's law with varying alloy concentrations inside the interface region over a distance w that can be adjusted depending on the abruptness of the simulated junction (see Methods in Supporting Information for more details and generalizations). Inside relatively abrupt junctions, corresponding to our experimental case, the drift velocity can be approximated by:

$$\vec{v}^*(x,y) \simeq \vec{v_0}^*(w)\left(1+\frac{x}{\Xi}\right) \quad , \quad 0 \le x \le w \quad (2)$$

where $\vec{v_0}^*(w) = -\frac{\mu}{w}(\Delta E - b_g)\hat{\mathbf{x}}$ is the drift velocity at the origin of the x axis (Refer to the frame $(\hat{\mathbf{x}}, \hat{\mathbf{y}})$ in Figure 1b), μ is the exciton mobility inside the interface, b_g is the band gap bowing parameter (see Methods in Supporting Information for details) and $\hat{\mathbf{x}}$ is the unit vector along the x-direction. The characteristic bowing distance is denoted by $\Xi = w(\Delta E - b_g)/(2b_g)$. Finally, on the left-hand side of Equation (1), the second and last term represent the recombination rate per time unit and the exciton photo-generation rate Γ (per unit of area and unit of time), respectively. The photo-generation rate spatial dependence is approximated by a 2D Gaussian profile, mimicking the laser excitation profile.

The steady-state exciton density in each position can be calculated as the excitation laser approaches the junction. However, in order to directly compare the theoretical predictions with experiments, we calculated the μ-PL images by convoluting the exciton density by a microscope objective-related Gaussian point spread function (PSF) (see Methods in Supporting Information for details), related to the diffraction-limited spatial resolution of the objective at the emission wavelength. **Figure 3**a–e are the theoretical counterparts of the experimental results given in Figure 2a–e. Figure 3a top row thus shows the calculated μ-PL intensity patterns for the laser and junction positions that match the experimental ones. Figure 3a in the bottom row presents the integrated intensity profiles along the x-axis (red curves), calculated from the maps as the experimental profiles of Figure 2a. Notice that exciton density profiles are added (blue curves). To match the experimental observations mentioned above, the theoretical width of the heterojunction was chosen to be very narrow ($w = 3$ nm). We set intrinsic diffusion coefficients and lifetimes in Equation 1 to the experimental effective values measured at room temperature by time-resolved PL spectroscopy (TRPL)[17,19,27]: $D_{WSe_2} \simeq 1\ cm^2.s^{-1}$, $D_{MoSe_2} \simeq 4\ cm^2.s^{-1}$, $\tau_{WSe_2} \simeq 80$ ps and $\tau_{MoSe_2} \simeq 50$ ps. Finally, to match the relative integrated PL intensity ratio observed experimentally (see Figure 2b), the ratio of exciton generation rate amplitude is set as $\Gamma_0^{WSe_2} = 3\Gamma_0^{MoSe_2}$. To decrease the number of free parameters accounted for the simulation, we fixed the thin interface properties by setting averaged values: $D_{interface} \simeq (D_{MoSe_2} + D_{WSe_2})/2$, $\tau_{interface} \simeq (\tau_{MoSe_2} + \tau_{WSe_2})/2$ and $\Gamma_0^{interface} = (\Gamma_0^{WSe_2} + \Gamma_0^{MoSe_2})/2$. This choice of approximation is supported by previous studies that suggest that in such high-quality and sharp junctions, no drastic changes in diffusion parameters are expected.[17–20]

One can clearly see that both experimental (Figure 2a) and theoretical (Figure 3a) images are in excellent agreement. All the previously described modifications of the μ -PL intensity patterns linked to the junction (shape, FWOHM, number of maxima and amplitude) are captured by the model. The progressive increase in broadening and the appearance of two distinct peaks of varying amplitude can be seen in positions (2), (3), and (4). The abrupt shrinkage of the spot size and the shift in position (5) are also well reproduced. Figures 3b and c show the color maps obtained from

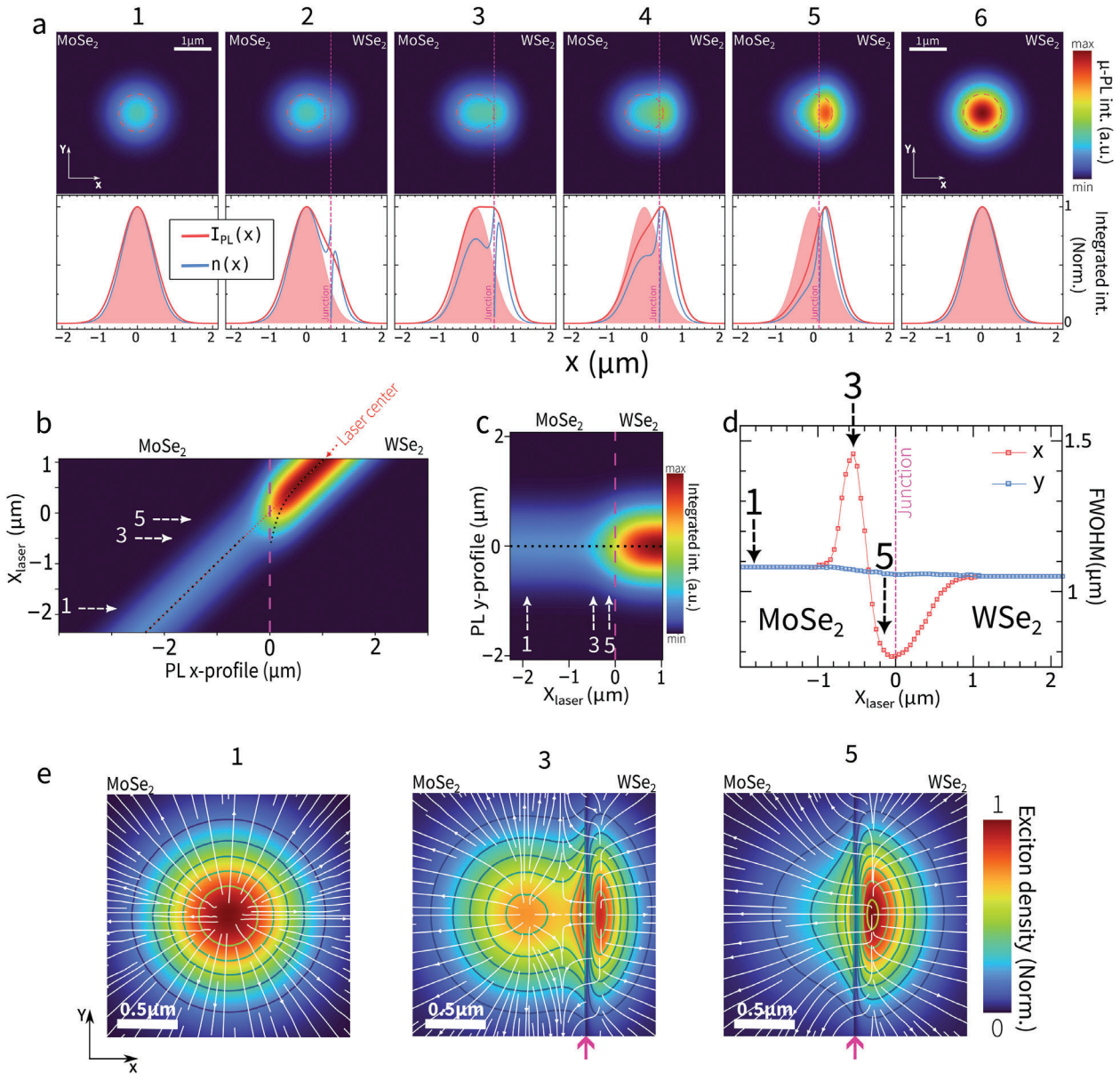

Figure 3. Modeling the exciton diffusion through the junction. a) top row: steady-state μ-PL images matching the experimental image positions (1) to (6), obtained by convolution of the calculated steady-state exciton distribution with an objective-related Gaussian PSF. The dashed red circle, with a diameter of $FWHM \sim 1\mu m$, indicates the position of the excitation laser spot, and the dashed pink line indicates the position of the junction separating $MoSe_2$ and WSe_2; bottom row: integrated μ-PL intensity profiles $I_{PL}(x, x_{laser}) = \int dy I_{PL}(x, y, x_{laser})$ (red curves) taken from the corresponding intensity maps, and x-axis profiles of the exciton density $n(x, x_{laser}) = \int dy n(x, y, x_{laser})$ (blue); the red shaded areas show the laser excitation profile. b) The color map obtained from the integrated μ-PL intensity $I_{PL}(x, x_{laser}) = \int dy I_{PL}(x, y, x_{laser})$ profiles as a function of the position of the excitation source (the center of the laser spot shown by the red dotted line), the vertical dashed line represents the separation between the two materials. Notice the two maxima around the interface. c) Same as (b) but for μ-PL intensity $I_{PL}(y, x_{laser}) = \int dx I_{PL}(x, y, x_{laser})$). d. FWOHMs extracted from the x-axis (red) and y-axis (blue) integrated μ-PL intensity profiles. e. Normalized exciton density color maps were calculated for positions (1), (3), and (5). The colored contours represent the isodensity curves. The white streamlines indicate the orientation of the exciton flux, showing the isotropic diffusion far from the junction (1) to a highly oriented flux (5). The pink arrow indicates the position of the junction.

the theoretical integrated μ-PL intensities profiles $I_{PL}(x, x_{laser}) = \int dy I_{PL}(x, y, x_{laser})$ and $I_{PL}(y, x_{laser}) = \int dx I_{PL}(x, y, x_{laser})$, respectively. Again, they are in excellent agreement with the experimental ones shown in Figure 2c,d, respectively. This confirms that our model describes very well both exciton diffusion and recombination for any position of the excitation.

3. Discussion

3.1. One Interface: Exciton Distribution and Flux

Having access to the exciton spatial distribution helps us understand how exciton Kapitza resistance at the junction affects the

PL emission in the optical far field configuration. When excitons are approaching the junction, two scenarios occur depending on whether excitons are generated in WSe_2 or in $MoSe_2$. In the first case, excitons are strongly drifted toward and perpendicularly to the junction, while in the second case, they are blocked by this junction. This creates for all calculated configurations a strong discontinuity of the exciton density (see blue profiles in Figure 3a bottom row), which can be described by a very high-density spot situated near the junction on the $MoSe_2$ side and, on the WSe_2 side, a mirroring minimum adjacent to the junction followed by a second maximum of exciton density. The modification of the relative amplitude of those three specific density features depending on the position of the laser source is at the origin of the observed complex behavior. Figure 3d shows the FWOHM for the integrated intensity profiles calculated on the *x*-axis (red curve) and *y*-axis (blue curve) as a function of the position of the excitation source. Compared with the experimental data shown in Figure 2e, the model captures very well both the diffusion regimes described above, confirming i) that in the enhanced diffusion regime, the interaction with the LH results in an enhanced effective diffusion length and ii) that in the forced diffusion regime, excitons are forced to diffuse toward a smaller area than the one they are excited in, resulting in an increase in exciton density compared to the isotropic case. However, one can see that the agreement between experiment and simulation, while still fairly good, is not perfect. In that case, the simulation slightly misses the laser position (x_{laser}) at which the FWOHM minimum of the x-axis profile takes place. We believe that as the exciton density strongly increases locally at the junction, both Auger recombination and emission/reabsorption of hot phonons occur. This should play a non-negligible role in causing an extra thermal drift of excitons (Seebeck effect),[28] which slightly broadens the experimental diffusion profiles (compared to the calculation).

Finally, we point out that our model not only describes very well the experimental results but also gives us access to the steady-state exciton flux, $\vec{\phi}(\mathbf{r}, \mathbf{r}_s) = -D(\mathbf{r})\vec{\nabla}n(\mathbf{r}, \mathbf{r}_s)$, deduced from the calculated exciton density, which allows us to predict the exciton average trajectories. Figure 3e depicts the normalized exciton density color maps for positions (1), (3), and (5). Colored contours and white streamlines represent the exciton isodensity curves and exciton flux orientations, respectively. As expected, far from the junction (see color map (1)), the diffusion is isotropic, as shown by both circular isodensity curves and radial flux lines. However, one can see that near the junction, the diffusion is profoundly affected. The junction has a significant impact on the exciton flux, redirecting it perpendicularly to the junction, and the exciton isodensity curves are no longer circular. In the enhanced diffusion regime (see color map (3)), it is obvious that the exciton flux imposed by the junction creates an exciton distribution presenting two separated maxima, in agreement with previous observations such as the μ-PL maxima (Figures 2a and 3a). One of the maxima (on the $MoSe_2$ side) is linked to the very high exciton generation inside the $MoSe_2$ layer at the center of the laser spot. The second one appears right at the junction on the WSe_2 side. At this position, the laser power density is much weaker than at the laser center, but due to the larger exciton generation rate of WSe_2, the two maxima are of comparable amplitude. Looking at the exciton flux distribution, it appears that this splitting of the exciton distribution is due to the competition between: i) the junction generated parallelized exciton flux originating from the WSe_2 side and perpendicularly to it (this region with nearly parallel flux lines extending approximately ≈250 nm away from the junction), and ii) the diffusion originating from the first hot spot in $MoSe_2$. Those two opposing fluxes block the exciton diffusion toward the interface area, generating, in the $n(\boldsymbol{r})$ distribution, a low-intensity saddle point between the two high exciton density spots. In the forced diffusion regime (see color map (5)), one can see that the parallelized exciton flux generated by the junction is even more predominant. As the laser center is now located nearly at the junction, the above-described competition between two hot spots does not occur, and nearly parallel flux lines are now found nearly 1μm away from the exciton source. In both described diffusion regimes, the exciton flux near the junction is one order of magnitude greater than the one calculated away from it.

3.2. Two Interfaces: Collimation and Focusing

We now study a more complex interface geometry that is naturally found in our samples. The tips of the $MoSe_2$ stars form triangles with two tilted junctions, crossing at a 60° angle, as illustrated in **Figure 4a**. As the laser excitation crosses the triangular interface, moving from $MoSe_2$ to WSe_2, we obtain μ-PL images experimentally and numerically using our model (two examples are given for two laser positions in insets of Figure 4b). Note that there is no change in energy and broadening of the excitonic contributions of each material, confirming a very sharp triangular interface. The FWOHM of the *x*- and *y*-axes profiles of the μ-PL intensity are shown in Figure 4b in red and blue, respectively. The experiment (top panel) and theory (bottom panel) are in very good agreement. Contrary to the behavior described above, where the forced and enhanced diffusion regimes are both found along the *x*-direction for different positions of the laser center (with very little variation along *y*-direction), here the specific interface geometry projects both phenomena onto the different directions. The forced diffusion regime is now only found along the *x*-axis, while enhanced diffusion (with FWOHM reaching ≈1.8μ*m*) occurs mainly along the *y*-axis. Note that the triangular structure is more efficient in enhancing the effective diffusion length than the straight one, with a PL diffusion spot reaching ≈1.9μ*m*. The resulting diffusion is therefore even more anisotropic than in the straight junction, with the possibility of independently affecting the effective diffusion length of the *x*- and *y*-axis. μ-PL color maps in insets of Figure 4b and predicted exciton distribution in Figure 4c illustrate clearly this behavior. In configuration 1, a distinct split of the μ-PL spot is visible, with two separate PL hot spots that appear at the interface. The exciton density observed at these two points is high. We point out that the distance between the two hot spots can be controlled, as it depends only on the distance between the two interfaces. In configuration 2, the FWOHM is reduced along the *x* -axis while increasing along the *y* -axis resulting in a strongly oblong PL spot.

Figure 4c also shows the calculated exciton flux orientation (white streamlines). The exciton flux strongly depends on the position of the excitation source. Indeed, as excitons are transmitted through the junction, their trajectories are modified by the peculiar geometry of the interface. In configuration 2, the

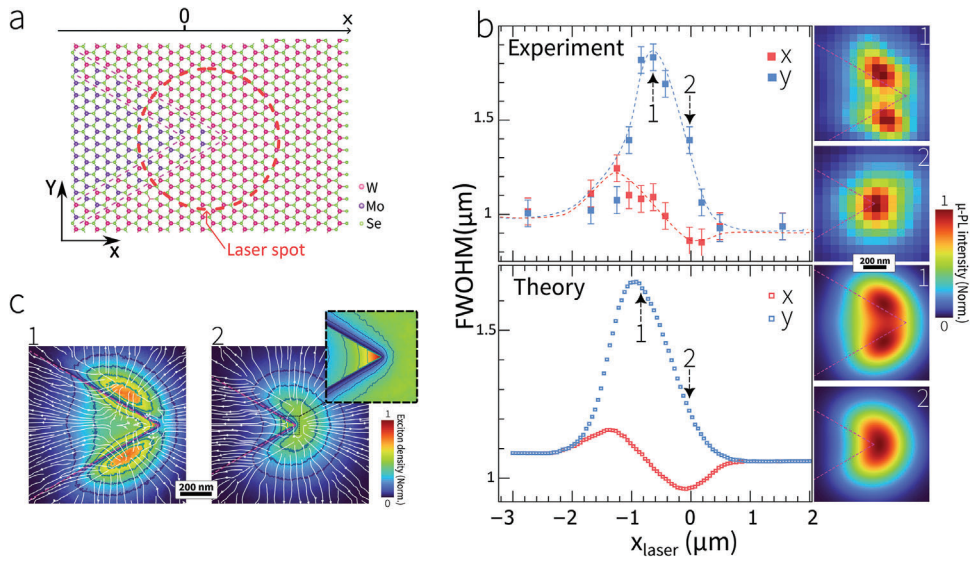

Figure 4. Exciton diffusion through a triangular interface. a) A schematic illustration of a triangular interface. The pink dashed lines indicate a thin alloy separating $MoSe_2$ and WSe_2 materials. b) top panel: Experimental FWOHM of the x-axis (red square) and y-axis (blue square) profiles as a function of the position of the laser center. The dashed lines are guides for the eyes. Insets show μ-PL images taken near the apex of the $MoSe_2$ triangle at positions 1 and 2, with the center of the laser spot being located at the center of the color maps. b) bottom panel: same as the top panel but for simulated μ-PL profiles. c) Calculated exciton distribution and exciton flux orientation for a triangular junction with the laser source placed at positions 1 and 2 shown in (b) bottom panel.

laser is placed at the triangle apex. As expected, excitons that are not interacting with the junction are diffusing isotropically with circular isodensity curves and radial flux lines. In contrast, the trajectories of excitons approaching the junction are modified as they acquire an extra component to their velocity perpendicular to the interface. Because of the triangular shape of the interface, excitons transmitted through the bottom and top interfaces are pushed toward the same point in space close to the apex (inside $MoSe_2$). In the inset of Figure 4c, this is clearly visible as a region of space near the triangular apex, which clearly presents a high density of convex isodensity curves, indicating converging trajectories leading to an increased exciton density. We would like to point out that with such a high-density gradient localized at the triangle apex, the resulting exciton diffusion away from the corner is very efficient. Generating such an exciton distribution at equilibrium is only possible because the junction, by altering the excitonic flux over large distances, is capable of draining a large number of excitons toward this small area.

Moving further away to the left from the apex, excitons present collimated average trajectories with excitons moving away from the source (inside $MoSe_2$) following nearly perfectly parallel average trajectories as far as $\approx 1.5 \mu m$ away from the source (up to the left edge of the color map). Recalling the configuration described in Figure 3 map (5) that already presented parallelized flux lines, one can see that the triangular interface is much more efficient at maintaining a collimated exciton flux over large distances. In configuration 1, the laser is now centered ≈300 nm inside $MoSe_2$ and one can see here a similar feature to the one described above but in a less optimal way. Indeed, first, the area of space where excitons are pushed together is larger, resulting in a lower local exciton density. Second, looking at the white streamlines away from the source, it is obvious that it is less efficient at converting the divergent excitonic trajectories into a set of parallel flux lines. This indicates that controlling the position of the exciton sources relative to the triangular interface tip gives the possibility of tuning the degree of divergence of the exciton flux lines.

3.3. Three Interfaces: Exciton Funneling and Trapping

Finally, the last key feature that we will focus on for this type of system is the ability to trap and confine neutral excitons within a controllable-size area. In fact, the efficient unidirectional exciton transport and trapping we demonstrated above suggests that a triangle-shaped $MoSe_2$ island surrounded by WSe_2 material should lead to huge amounts of excitons being forced into the $MoSe_2$ triangle and then trapped inside. Reducing the size of a small $MoSe_2$ triangle will then lead to an increasing exciton population that occupies a decreasing area. We performed μ-PL imaging on a small $MoSe_2$ triangle of size inferior to the laser spot size found in our sample (Tip-enhanced Raman characterization is given in Figure 2c). To obtain spatially resolved information from the μ-PL spectra, and as described in Methods in Supporting Information, we added a 75 μm large pinhole. In such a configuration, due to the μ-scope magnification, the signal is collected only over a circular area of ≈750 nm centered at the laser spot center. In **Figure** 5a, the blue spectrum is measured with the pinhole, where only the photons emitted by excitons recombining inside a ≈750 nm diameter circle centered on the laser center are collected, while the red spectrum corresponds to the spectra measured without the pinhole, where all photons are collected independently of the position of emission. One can clearly see that the contribution of $MoSe_2$ excitons remains the same in both spectra (the spectra are not re-normalized), indicating first that the $MoSe_2$ island is smaller than the area delimited by the collection and, second, that very few excitons are recombining

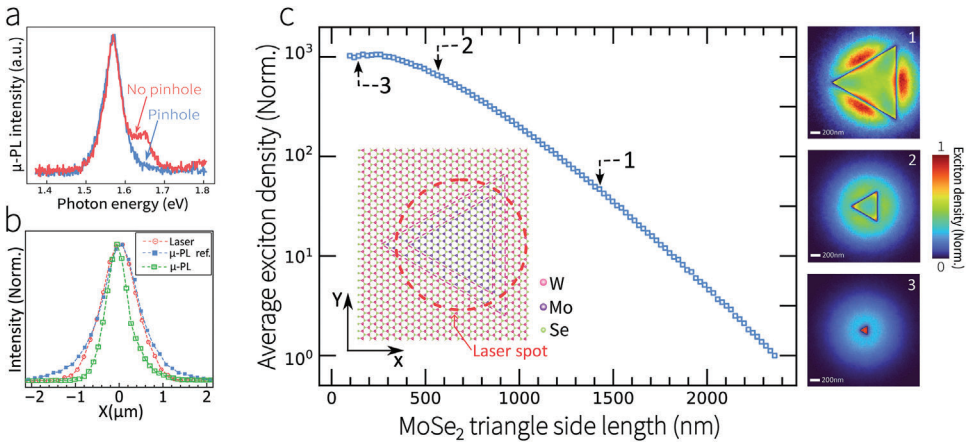

Figure 5. Exciton trapping in sub-wavelength sized $MoSe_2$ triangles a) μ-PL spectra taken with the laser being centered at the centroid of the $MoSe_2$ triangle with the pinhole (blue spectrum) and without the pinhole (red spectrum). b) x-axis profile of the laser intensity (red curve) and μ-PL intensity (green curve) with the excitation laser being centered on the small $MoSe_2$ triangle characterized in Figure S2 (Supporting Information). As a reference, the profile of the isotropic case taken away from the junction inside the $MoSe_2$ is given in blue. c) Calculated average exciton density inside the $MoSe_2$ triangle versus the triangle side length with the excitation laser centered at the centroid of the $MoSe_2$ triangle as illustrated in the inset. The color maps show the exciton density calculated for cases 1, 2, and 3. For clarity, the three false-color insets are individually normalized.

inside WSe_2. This is surprising because, due to the small size of the $MoSe_2$ island, a non-negligible portion of the laser shines directly on WSe_2, seemingly indicating that excitons are being trapped inside $MoSe_2$. This is confirmed by the measured integrated intensity profiles along the x-axis (measured as described above in Section 2.1) plotted in green in Figure 5b, where the μ-PL intensity extends less than the x-axis profile measured in the isotropic case (i.e. away from the junction) inside $MoSe_2$ (blue curve) and even than the laser excitation profile (red curve), proving that excitons are being forced to diffuse from the excitation inside a smaller $MoSe_2$ triangle, de facto concentrating excitons.

To go further, in Figure 5c, we display the expected average exciton density calculated with our model inside a $MoSe_2$ equilateral triangle versus the side length of the triangle (with the laser-centered on the $MoSe_2$ triangle centroid as illustrated in the inset). A strong increase is evidenced by decreasing the triangle size, the resulting average exciton density inside the $MoSe_2$ triangle is increased by three orders of magnitude when the triangle side is reduced from 2500 to 100 nm. This clearly illustrates the ability of the small $MoSe_2$ triangle to drag and trap excitons from surrounding WSe_2 over large distances. It is interesting to look at the local exciton distribution as the triangle decreases in size (see insets in Figure 5c). In inset 1, the triangle is of comparable size with the laser spot, and the density maxima appear along the three edges, with an exciton transport dominated by the enhanced regime described in Section 1 pushing excitons toward the triangle centroid. In inset 2, when the triangle edges become smaller than ≈1 μm, the maxima of exciton density are moved to the triangle apexes, with an exciton transport dominated by the "lensing" effect described in Section 2. In inset 1, for a small triangle, a more homogeneous exciton distribution is observed as hot spots start to merge. Figure S2d (Supporting Information) shows the same color maps but normalized to the same value. Note that small $MoSe_2$ triangles isolate and homogenize a high density of photo-generated excitons, making them a promising platform for investigating new collective excitonic effects. Finally, we emphasize that the results shown here are only a proof of concept and have inherent limitations. Indeed, as all calculations are made assuming the linear regime, if the resulting local exciton density generated inside the $MoSe_2$ triangle becomes high enough to generate non-negligible non-linear behavior, such as exciton–exciton annihilation, the predicted dependence will no longer be correct.

4. Conclusion

In summary, room-temperature μ-PL imaging on high-quality WSe_2-$MoSe_2$ LH combined with a theoretical study based on a statistical approach of exciton diffusion were performed. In the low exciton density regime, we shed light on the in-plane exciton flux control offered by TMD heteromonolayers. Our work demonstrates that the abrupt change in exciton energy transforms the 2D isotopic diffusion into a strong anisotropic diffusion pattern along the direction perpendicular to the junction, drastically affecting the effective diffusion length in a given direction, forcing either excitons to spread over large distances or, on the contrary, pushing them together to create a high-density hot spot. Going further, we show that combining two of the straight interfaces to form a triangle can act as an "excitonic lens," which is able, for a specific position of the source, to collimate the naturally diverging exciton flux into a beam of parallel-propagating excitons. Finally, we show that $MoSe_2$ triangles embedded in a WSe_2 matrix with sub-wavelength sizes ranging from a few dozen to a few hundred nanometers are highly efficient systems for trapping and confining excitons in adjustable-size spaces. Our findings reveal a set of refraction-like rules that describe global changes in global trajectories as a neutral exciton change medium. We explored experimentally and theoretically three different naturally occurring geometries and described the diverse possibilities offered by this type of system. As such, we believe that this work has the potential to open the door to a wide range of emerging quantum applications in designing new excitonic

technologies, such as new collective excitonic phenomena, exciton Bose–Einstein condensate, and exciton quantum dots-based applications.

Supporting Information

Supporting Information is available from the Wiley Online Library or from the author.

Acknowledgements

This work was financially supported by ANR Ti-P (ANR-21-CE30-0042), the Deutsche Forschungsgemeinschaft (DFG) through a research infrastructure grant CRC 1375 NOA (Project B2, 398816777), SPP2244 (Project TU149/21-1, 443361515) and DFG individual grant TU149/16-1 (464283495).

Conflict of Interest

The authors declare no conflicts of interest.

Data Availability Statement

The data that support the findings of this study are available from the corresponding author upon reasonable request.

Keywords

exciton diffusion, exciton transfer, exciton control, exciton flux, exciton kapitza resistance, excitronics, lateral heterostructure, transition metal dichalcogenide

Received: November 5, 2024
Revised: December 6, 2024
Published online:

[1] G. Wang, A. Chernikov, M. M. Glazov, T. F. Heinz, X. Marie, T. Amand, B. Urbaszek, *Rev. Mod. Phys.* **2018**, *90*, 021001.
[2] M. Koperski, M. R. Molas, A. Arora, K. Nogajewski, A. O. Slobodeniuk, C. Faugeras, M. Potemski, *Nanophotonics* **2017**, *6*, 1289.
[3] D. Y. Qiu, T. Cao, S. G. Louie, *Phys. Rev. Lett.* **2015**, *115*, 176801.
[4] A. Steinhoff, M. Rosner, F. Jahnke, T. O. Wehling, C. Gies, *Nano Lett.* **2014**, *14*, 3743.
[5] E. Malic, M. Selig, M. Feierabend, S. Brem, D. Christiansen, F. Wendler, A. Knorr, G. Berghäuser, *Phys. Rev. Mater.* **2018**, *2*, 014002.
[6] R. C. Miller, A. C. Gossard, W. T. Tsang, *Phys. B+C* **1983**, *117-118*, 714.
[7] P. Rivera, H. Yu, K. L. Seyler, N. P. Wilson, W. Yao, X. Xu, *Nat. Nanotechnol.* **2018**, *13*, 1004.
[8] A. A. High, E. E. Novitskaya, L. V. Butov, M. Hanson, A. C. Gossard, *Science* **2008**, *321*, 229.
[9] Y. Chen, W. Yao, Z. Liu, J. Hu, J. Li, D. Li, *Adv. Phys. Res.* **2023**, 2200083.
[10] R. Peng, A. Ripin, Y. Ye, J. Zhu, C. Wu, S. Lee, H. Li, T. Taniguchi, K. Watanabe, T. Cao, X. Xu, M. Li, *Nat. Commun.* **2022**, *13*, 1334.
[11] Y. Hu, F. Zhang, M. Titze, B. Deng, H. Li, G. J. Cheng, *Nanoscale* **2018**, *10*, 5717.
[12] F. Dirnberger, J. D. Ziegler, P. E. Faria Junior, R. Bushati, T. Taniguchi, K. Watanabe, J. Fabian, D. Bougeard, A. Chernikov, V. M. Menon, *Sci. Adv.* **2021**, *7*, eabj3066.
[13] C. Chakraborty, N. Vamivakas, D. Englund, *Nanophotonics* **2019**, *8*, 2017.
[14] M. Yagmurcukardes, Y. Qin, S. Ozen, M. Sayyad, F. M. Peeters, S. Tongay, H. Sahin, *Appl. Phys. Rev.* **2020**, *7*, 1.
[15] Y. Liu, N. O. Weiss, X. Duan, H.-C. Cheng, Y. Huang, X. Duan, *Nat. Rev. Mater.* **2016**, *1*, 1.
[16] E. Najafidehaghani, Z. Gan, A. George, T. Lehnert, G. Q. Ngo, C. Neumann, T. Bucher, I. Staude, D. Kaiser, T. Vogl, et al., *Adv. Funct. Mater.* **2021**, *31*, 2101086.
[17] D. Beret, I. Paradisanos, H. Lamsaadi, Z. Gan, E. Najafidehaghani, A. George, T. Lehnert, J. Biskupek, U. Kaiser, S. Shree, A. Estrada-Real, D. Lagarde, X. Marie, P. Renucci, K. Watanabe, T. Taniguchi, S. Weber, V. Paillard, L. Lombez, J.-M. Poumirol, A. Turchanin, B. Urbaszek, *npj 2D Mater. Appl.* **2022**, *6*, 84.
[18] M. Shimasaki, T. Nishihara, K. Matsuda, T. Endo, Y. Takaguchi, Z. Liu, Y. Miyata, Y. Miyauchi, *ACS nano* **2022**, *16*, 8205.
[19] H. Lamsaadi, D. Beret, I. Paradisanos, P. Renucci, D. Lagarde, X. Marie, B. Urbaszek, Z. Gan, A. George, K. Watanabe, T. Taniguchi, A. Turchanin, L. Lombez, N. Combe, V. Paillard, J.-M. Poumirol, *Nat. Commun.* **2023**, *14*, 5881.
[20] M. Shimasaki, T. Nishihara, N. Wada, Z. Liu, K. Matsuda, Y. Miyata, Y. Miyauchi, *Appl. Phys. Express* **2023**, *16*, 012010.
[21] S. Ambardar, R. Kamh, Z. H. Withers, P. K. Sahoo, D. V. Voronine, *Nanoscale* **2022**, *14*, 8050.
[22] M. Khan, M. N. Tripathi, A. Tripathi, *Mater. Sci. Semicond. Process.* **2024**, *177*, 108339.
[23] Y. Zhou, G. Scuri, D. S. Wild, A. A. High, A. Dibos, L. A. Jauregui, C. Shu, K. De Greve, K. Pistunova, A. Y. Joe, et al., *Nat. Nanotechnol.* **2017**, *12*, 856.
[24] G. Wang, C. Robert, M. M. Glazov, F. Cadiz, E. Courtade, T. Amand, D. Lagarde, T. Taniguchi, K. Watanabe, B. Urbaszek, et al., *Phys. Rev. Lett.* **2017**, *119*, 047401.
[25] J.-M. Poumirol, I. Paradisanos, S. Shree, G. Agez, X. Marie, C. Robert, N. Mallet, P. R. Wiecha, G. Larrieu, V. Larrey, et al., *ACS photonics* **2020**, *7*, 3106.
[26] R. Rosati, I. Paradisanos, L. Huang, Z. Gan, A. George, K. Watanabe, T. Taniguchi, L. Lombez, P. Renucci, A. Turchanin, et al., *Nat. Commun.* **2023**, *14*, 2438.
[27] J. Zipfel, M. Kulig, R. Perea-Causín, S. Brem, J. D. Ziegler, R. Rosati, T. Taniguchi, K. Watanabe, M. M. Glazov, E. Malic, et al., *Phys. Rev. B* **2020**, *101*, 115430.
[28] R. Perea-Causin, S. Brem, R. Rosati, R. Jago, M. Kulig, J. D. Ziegler, J. Zipfel, A. Chernikov, E. Malic, *Nano Lett.* **2019**, *19*, 7317.